

An Upwind Differencing Scheme for the Incompressible Navier-Stokes Equations

Stuart E. Rogers and Dochan Kwak
NASA Ames Research Center, Moffett Field, CA 94035-1000, USA

Originally appeared as NASA TM 101051, November 1988
Published in *Applied Numerical Mathematics*, Vol. 8, 1991, pp. 43–64.

Abstract

The steady-state incompressible Navier-Stokes equations in two-dimensions are solved numerically using the artificial compressibility formulation. The convective terms are upwind differenced using a flux-difference split approach that has uniformly high accuracy throughout the interior grid points. The viscous fluxes are differenced using second-order accurate central differences. The numerical system of equations is solved using an implicit line relaxation scheme. The scheme is applicable to both steady-state and unsteady flow computations. In the current work steady-state applications are emphasized. Characteristic boundary conditions are formulated and used in the solution procedure. The overall scheme is capable of being run at extremely large pseudo-time steps, leading to fast convergence. Three test cases are presented to demonstrate the accuracy and robustness of the code. These are the flow in a square driven cavity, flow over a backward facing step, and flow around a two-dimensional circular cylinder.

1. Introduction

The overall motivation for the current work is a desire to find an efficient method of solution for the incompressible Navier-Stokes equations for complex three-dimensional (3D) geometries. To this end, the present study looks at applying an upwind differencing scheme in conjunction with the pseudocompressibility method. This method was first introduced by Chorin [1] and has been used with much success by Kwak *et al* [2] for solving complex incompressible flow problems in generalized coordinates. In this formulation, a time derivative of pressure is added to the continuity equation. Together with the momentum equations, this forms a hyperbolic system of equations which can be marched in pseudo-time to a steady-state solution. The method can also be extended to solve time-dependent problems [3,4] by using subiterations in pseudo-time at every physical time step. If all that is desired is the steady-state solution to a problem the pseudocompressibility method can be a very efficient formulation because it does not require that a divergence free velocity field be obtained at each iteration. The addition of the time derivative of pressure to the continuity creates a hyperbolic system of equations complete with artificial pressure waves of finite speed. When the solution converges to a steady-state, a divergence free solution is obtained. Since this is the case, many of the well-developed compressible flow algorithms can be utilized for this method.

Many previous applications of this method have used central differencing of the convective fluxes. This approach also requires that artificial dissipation be explicitly added in order to damp out the spurious oscillations which are due to the nonlinearity of the convective fluxes. Such a scheme can be difficult to apply as the artificial dissipation parameters must be adjusted for each specific calculation. The use of too much artificial dissipation will also tend to hamper the accuracy of the calculations [5]. In order to avoid these problems associated with central differencing, an upwind differencing scheme is considered here. While upwind differencing does add artificial viscosity, it does so based on the physics of the problem and does not require the user to specify an artificial viscosity parameter. Of most recent interest have been the class of upwind-differencing schemes which

bias the differencing based on the sign of the eigenvalues of the convective flux Jacobians. A number of these types of schemes have been developed in conjunction with solving the Euler equations and the compressible Navier-Stokes equations [6-9]. The development of these schemes base the upwind differencing on the physics of the Riemann problem. In the case of the pseudocompressibility method the upwind differencing is merely a way of using the physics of the artificial waves to obtain a smooth numerical solution.

Much of the current development of upwind-differencing schemes has focused on the ability to resolve sharp discontinuities without kinks or overshoots. By limiting the order of the differencing at points near the discontinuities, and thereby increasing the dissipation provided by the differencing, the schemes have the total variation diminishing (TVD) property. Applications of TVD schemes to the incompressible equations were done by Hartwich and Hsu [10,11] and Gorski [12]. These investigators were able to obtain 3D solutions which were third order accurate in the convective terms, except near regions of large change in gradient, where the order of the differencing was reduced in order to increase the amount of dissipation added.

Since solutions to the incompressible equations do not have strong discontinuities such as shocks, it is reasoned that the incompressible equations could be solved without the need for any limiting, and that flux-difference splitting of uniformly high order could be used. This paper attempts to show that this is so by using a flux-difference splitting type of formulation similar to that used for compressible flow in [6,7]. The current work concentrates on the development of this scheme with the use of a two-dimensional (2D) flow solver using fifth-order upwind differencing of the convective terms. Since the development of the upwind-differencing schemes considered here are based upon an analysis of a one-dimensional hyperbolic conservation law, the use of a 2D code for the initial testing done here will not be out of line from the desired goal of a 3D algorithm. This will expedite much of the code development because of the smaller computational requirements of a 2D code and because of the relative ease with which 2D results can be analyzed, compared, and presented.

In the following sections, the details of the 2D code are presented, including the governing equations and the similarity transformation for the Jacobian matrix of the convective fluxes. The specific details of the upwind scheme are given, followed by the details of the implicit line relaxation scheme used to solve the equations. Some boundary conditions based on the method of characteristics have been developed, and are presented. The computed results section shows the robustness and accuracy of the code by presenting three sample problems, the flow inside a driven cavity, the flow over a backward facing step, and the flow over a circular cylinder.

2. Governing Equations

The equations governing constant density viscous flow are presented here in nondimensional form. Following the pseudocompressibility formulation a time derivative of pressure is added to the continuity equation resulting in

$$\frac{\partial p}{\partial \tau} + \beta \left(\frac{\partial u}{\partial x} + \frac{\partial v}{\partial y} \right) = 0 \quad (1)$$

where u and v are velocity components in the x and y directions, respectively, and β is known as the pseudocompressibility constant. Here, τ represents pseudo-time and is not related in any way with physical time. Combining Eq. (1) with the momentum equations for the incompressible Navier-Stokes equations results in the following system in Cartesian coordinates

$$\begin{aligned}
\frac{\partial}{\partial \tau} D + \frac{\partial}{\partial x}(E - E_v) + \frac{\partial}{\partial y}(F - F_v) &= 0 \\
D &= \begin{bmatrix} p \\ u \\ v \end{bmatrix} \quad E = \begin{bmatrix} \beta u \\ u^2 + p \\ uv \end{bmatrix} \quad F = \begin{bmatrix} \beta v \\ uv \\ v^2 + p \end{bmatrix} \\
E_v &= \begin{bmatrix} 0 \\ \tau_{xx} \\ \tau_{xy} \end{bmatrix} \quad F_v = \begin{bmatrix} 0 \\ \tau_{yx} \\ \tau_{yy} \end{bmatrix} \\
\tau_{xx} &= 2\nu \frac{\partial u}{\partial x} \quad \tau_{yy} = 2\nu \frac{\partial v}{\partial y} \\
\tau_{xy} &= \tau_{yx} = \nu \left(\frac{\partial u}{\partial y} + \frac{\partial v}{\partial x} \right)
\end{aligned} \tag{2}$$

where p is the pressure. In this formulation the Reynolds stress has been approximated as a function of the strain rate tensor, and thus ν represents a sum of the kinematic viscosity and the turbulent eddy viscosity. The equations in (2) are transformed into generalized curvilinear coordinates given by

$$\begin{aligned}
\xi &= \xi(x, y) \\
\eta &= \eta(x, y)
\end{aligned}$$

The equations are then given by

$$\frac{\partial}{\partial \tau} \hat{D} + \frac{\partial}{\partial \xi}(\hat{E} - \hat{E}_v) + \frac{\partial}{\partial \eta}(\hat{F} - \hat{F}_v) = 0; \quad \hat{D} = \frac{1}{J} \begin{bmatrix} p \\ u \\ v \end{bmatrix} \tag{3}$$

where J is the Jacobian of the transformation, the metrics of the transformation are

$$\xi_x = \frac{\partial \xi}{\partial x}, \quad \eta_y = \frac{\partial \eta}{\partial y}, \quad \text{etc.}$$

and the convective fluxes are given by

$$\hat{E} = \frac{1}{J} \begin{bmatrix} \beta U \\ uU + \xi_x p \\ vU + \xi_y p \end{bmatrix} \quad \hat{F} = \frac{1}{J} \begin{bmatrix} \beta V \\ uV + \eta_x p \\ vV + \eta_y p \end{bmatrix} \tag{4}$$

where the contravariant velocity components, U and V are defined as

$$\begin{aligned}
U &= \xi_x u + \xi_y v \\
V &= \eta_x u + \eta_y v
\end{aligned}$$

In deriving the viscous fluxes, constant viscosity was assumed for simplicity and because initially only laminar flow calculations are being performed. This simplification is not necessary and is easily removed. The viscous fluxes are given by

$$\begin{aligned}\hat{E}_v &= \frac{\nu}{J} \begin{bmatrix} 0 \\ (\xi_x^2 + \xi_y^2)u_\xi + (\xi_x\eta_x + \xi_y\eta_y)u_\eta \\ (\xi_x^2 + \xi_y^2)v_\xi + (\xi_x\eta_x + \xi_y\eta_y)v_\eta \end{bmatrix} \\ \hat{F}_v &= \frac{\nu}{J} \begin{bmatrix} 0 \\ (\xi_x\eta_x + \xi_y\eta_y)u_\xi + (\eta_x^2 + \eta_y^2)u_\eta \\ (\xi_x\eta_x + \xi_y\eta_y)v_\xi + (\eta_x^2 + \eta_y^2)v_\eta \end{bmatrix}\end{aligned}\quad (5)$$

where ν is the kinematic viscosity. If an orthogonal grid is assumed then the viscous fluxes reduce to

$$\hat{E}_v = \frac{\nu}{J} \begin{bmatrix} 0 \\ (\xi_x^2 + \xi_y^2)u_\xi \\ (\xi_x^2 + \xi_y^2)v_\xi \end{bmatrix} \quad \hat{F}_v = \frac{\nu}{J} \begin{bmatrix} 0 \\ (\eta_x^2 + \eta_y^2)u_\eta \\ (\eta_x^2 + \eta_y^2)v_\eta \end{bmatrix}\quad (6)$$

The upwind scheme requires the use of the eigensystem of the Jacobian matrix of the convective flux vectors. The two-dimensional eigensystem is presented here. For the three-dimensional equations, see Rogers *et al.* [13], or Hartwich and Hsu [10]. Beware, however, that the transformation given by the latter can become singular for certain values of metrics.

The generalized flux vector for the two-dimensional system of equations is given by

$$\hat{E}_i = \begin{bmatrix} \beta Q \\ uQ + k_x p \\ vQ + k_y p \end{bmatrix}\quad (7)$$

where $\hat{E}_i = \hat{E}, \hat{F}$ for $i = 1, 2$ respectively, and the metrics are represented with

$$\begin{aligned}k_x &= \frac{1}{J} \frac{\partial \xi}{\partial x}, \quad i = 1, 2 \\ k_y &= \frac{1}{J} \frac{\partial \xi}{\partial y}, \quad i = 1, 2\end{aligned}$$

where $\xi_1 = \xi$, $\xi_2 = \eta$, and the scaled contravariant velocity component is

$$Q = k_x u + k_y v$$

The Jacobian matrix of this generalized flux vector is given by

$$\hat{A}_i = \frac{\partial \hat{E}_i}{\partial D} = \begin{bmatrix} 0 & \beta k_x & \beta k_y \\ k_x & k_x u + Q & k_y u \\ k_y & k_x v & k_y v + Q \end{bmatrix}\quad (8)$$

A similarity transform for the Jacobian matrix is derived here of the form

$$\hat{A}_i = X_i \Lambda_i X_i^{-1}$$

where

$$\Lambda_i = \begin{bmatrix} Q & 0 & 0 \\ 0 & Q + c & 0 \\ 0 & 0 & Q - c \end{bmatrix} \quad (9)$$

and where c is the scaled artificial speed of sound given by

$$c = [Q^2 + \beta(k_x^2 + k_y^2)]^{1/2} \quad (10)$$

This variable will always be greater than Q and so the second eigenvalue will always be positive and the third eigenvalue will always be negative. The matrix of the right eigenvectors is given by

$$X_i = \frac{1}{2\beta c^2} \begin{bmatrix} 0 & c\beta & -c\beta \\ -2\beta k_y & u(c+Q) + \beta k_x & u(c-Q) + \beta k_x \\ 2\beta k_x & v(c+Q) + \beta k_y & v(c-Q) + \beta k_y \end{bmatrix} \quad (11)$$

and its inverse is given by

$$X_i^{-1} = \begin{bmatrix} k_y u - k_x v & -Qv - \beta k_y & Qu + \beta k_x \\ c - Q & \beta k_x & \beta k_y \\ -c - Q & \beta k_x & \beta k_y \end{bmatrix} \quad (12)$$

3. Upwind Differencing

Upwind differencing is used to numerically compute the convective flux derivatives. The upwind scheme is derived from one-dimensional (1D) considerations, and then is applied to each coordinate direction separately. Flux-difference splitting is used here to bias the differencing based on the sign of the eigenvalues of the convective flux Jacobian. The scheme as presented here was originally derived by Roe [7] as an approximate Riemann solver for the compressible gas dynamics equations.

The derivative of the convective flux in the ξ direction is approximated by

$$\frac{\partial E}{\partial \xi} \approx \frac{[\tilde{E}_{j+1/2} - \tilde{E}_{j-1/2}]}{\Delta \xi} \quad (13)$$

where $\tilde{E}_{j+1/2}$ is a numerical flux and j is the discrete spatial index for the ξ direction.

The numerical flux is given by

$$\tilde{E}_{j+1/2} = \frac{1}{2} \left[\hat{E}(D_{j+1}) + \hat{E}(D_j) - \phi_{j+1/2} \right] \quad (14)$$

For $\phi_{j+1/2} = 0$ this represents a second-order central difference scheme. The $\phi_{j+1/2}$ is a dissipation term. A first-order upwind scheme is given by

$$\phi_{j+1/2} = \Delta E_{j+1/2}^+ - \Delta E_{j+1/2}^- \quad (15)$$

where ΔE^\pm is the flux difference across positive or negative traveling waves. The flux difference is computed as

$$\Delta E_{j+1/2}^\pm = A^\pm(\bar{D})\Delta D_{j+1/2} \quad (16)$$

where the Δ operator is given by

$$\Delta D_{j+1/2} = D_{j+1} - D_j$$

The plus (minus) Jacobian matrix has only positive (negative) eigenvalues and is computed from

$$\begin{aligned} A^\pm &= X_1 \Lambda_1^\pm X_1^{-1} \\ \Lambda_1^\pm &= \frac{1}{2}(\Lambda_1 \pm |\Lambda_1|) \end{aligned} \quad (17)$$

This Jacobian matrix is evaluated using some intermediate value which is a function of the surrounding points, j and $j + 1$. The Roe properties [7] which are necessary for a conservative scheme, are satisfied if this is taken as the average of the surrounding values. Thus

$$\bar{D} = \frac{1}{2}(D_{j+1} + D_j) \quad (18)$$

A scheme of arbitrary order may be derived using these flux differences. Implementation of higher order accurate approximations in an explicit scheme do not require significantly more computational time if the flux differences ΔE^\pm are all computed at once for a single line. A third order upwind flux is defined by

$$\phi_{j+1/2} = -\frac{1}{3}[\Delta E_{j-1/2}^+ - \Delta E_{j+1/2}^+ + \Delta E_{j+1/2}^- - \Delta E_{j+3/2}^-] \quad (19)$$

The primary problem with using schemes of accuracy greater than third order occurs at the boundaries. Large stencils will require special treatment at the boundaries, and a reduction of order is necessary. Therefore, when going to a higher order accurate scheme, compactness is desirable. Such a scheme was derived by Rai [14] using a fifth-order accurate upwind-biased stencil. A fifth-order fully upwind difference would require 11 points, but this upwind-biased scheme requires only 7 points. It is given by

$$\begin{aligned} \phi_{j+1/2} = -\frac{1}{30} [& -2\Delta E_{j-3/2}^+ + 11\Delta E_{j-1/2}^+ - 6\Delta E_{j+1/2}^+ - 3\Delta E_{j+3/2}^+ \\ & + 2\Delta E_{j+5/2}^- - 11\Delta E_{j+3/2}^- + 6\Delta E_{j+1/2}^- + 3\Delta E_{j-1/2}^-] \end{aligned} \quad (20)$$

Next to the boundary, near second order accuracy can be maintained by the third and fifth order schemes by using the following

$$\phi_{j+1/2} = \epsilon \left[\Delta E_{j+1/2}^+ - \Delta E_{j+1/2}^- \right] \quad (21)$$

For $\epsilon = 0$, this flux leads to a second order central difference. For $\epsilon = 1$, this is the same as the first-order dissipation term given by Eq. (15). By including a nonzero ϵ , dissipation

is added to the second-order central difference scheme to help suppress any oscillations. A value of $\epsilon = 0.01$ is used for all of the results presented in this paper.

4. Implicit Scheme

This section describes the way in which Eq. (3) is numerically represented and solved. Application of a first order backward Euler formula to this system of equations yields the following delta form equation

$$\left[\frac{1}{J\Delta\tau}I + \left(\frac{\partial R}{\partial D} \right)^n \right] (D^{n+1} - D^n) = -R^n \quad (22)$$

where the superscript n is the pseudo-time iteration count and the vector R is the residual vector. Following the formula given in Eq. (13) and applying a second-order central difference formula to the viscous terms, at a point $x_{j,k}, y_{j,k}$ the numerical approximation to the residual vector is given by

$$R_{j,k} = \frac{\tilde{E}_{j+1/2,k} - \tilde{E}_{j-1/2,k}}{\Delta\xi} + \frac{\tilde{F}_{j,k+1/2} - \tilde{F}_{j,k-1/2}}{\Delta\eta} - \frac{(\hat{E}_v)_{j+1,k} - (\hat{E}_v)_{j-1,k}}{2\Delta\xi} - \frac{(\hat{F}_v)_{j,k+1} - (\hat{F}_v)_{j,k-1}}{2\Delta\eta} \quad (23)$$

where the numerical fluxes \tilde{E} and \tilde{F} are evaluated using Eq. (14) with either the first, third, or fifth order dissipation term given in Eqs. (15,19,20), respectively. The generalized coordinates are chosen so that $\Delta\xi$ and $\Delta\eta$ are equal to one.

The formation of the exact Jacobian matrix of the residual vector will be too expensive for practical consideration, particularly when higher-order upwind differencing is used, so the implicit side formulation will be limited to using the residual resulting from the first order upwind differencing. Applying the first order dissipation term in Eq. (15) to the convective terms, the residual is given by

$$R_{ij} = \frac{1}{2} \left[\hat{E}_{j+1,k} - \hat{E}_{j-1,k} - \Delta E_{j+1/2,k}^+ + \Delta E_{j+1/2,k}^- + \Delta E_{j-1/2,k}^+ - \Delta E_{j-1/2,k}^- + \hat{F}_{j,k+1} - \hat{F}_{j,k-1} - \Delta F_{j,k+1/2}^+ + \Delta F_{j,k+1/2}^- + \Delta F_{j,k-1/2}^+ - \Delta F_{j,k-1/2}^- - (\hat{E}_v)_{j+1,k} + (\hat{E}_v)_{j-1,k} - (\hat{F}_v)_{j,k+1} + (\hat{F}_v)_{j,k-1} \right] \quad (24)$$

The exact Jacobian matrix of the residual vector will form a banded matrix of the form:

$$\frac{\partial R}{\partial D} = \mathcal{B} \left[\frac{\partial R_{j,k}}{\partial D_{j,k-1}}, 0, \dots, 0, \frac{\partial R_{j,k}}{\partial D_{j-1,k}}, \frac{\partial R_{j,k}}{\partial D_{j,k}}, \frac{\partial R_{j,k}}{\partial D_{j+1,k}}, 0, \dots, 0, \frac{\partial R_{j,k}}{\partial D_{j,k+1}} \right] \quad (25)$$

where \mathcal{B} refers to a banded matrix. Using approximate Jacobians of the flux differences as derived and analyzed by Barth [15], the implicit side of the numerical equation is formed using the following terms

$$\begin{aligned}
\frac{\partial R_{j,k}}{\partial D_{j,k-1}} &\approx \frac{1}{2}(-\hat{B}_{j,k-1} - B_{j,k-1/2}^+ + B_{j,k-1/2}^-) + (\gamma_2)_{j,k-1} \\
\frac{\partial R_{j,k}}{\partial D_{j-1,k}} &\approx \frac{1}{2}(-\hat{A}_{j-1,k} - A_{j-1/2,k}^+ + A_{j-1/2,k}^-) + (\gamma_1)_{j-1,k} \\
\frac{\partial R_{j,k}}{\partial D_{j,k}} &\approx \frac{1}{2}(A_{j+1/2,k}^+ + A_{j-1/2,k}^+ - A_{j+1/2,k}^- - A_{j-1/2,k}^- \\
&\quad B_{j,k+1/2}^+ + B_{j,k-1/2}^+ - B_{j,k+1/2}^- - B_{j,k-1/2}^-) \\
\frac{\partial R_{j,k}}{\partial D_{j+1,k}} &\approx \frac{1}{2}(\hat{A}_{j+1,k} - A_{j+1/2,k}^+ + A_{j+1/2,k}^-) - (\gamma_1)_{j+1,k} \\
\frac{\partial R_{j,k}}{\partial D_{j,k+1}} &\approx \frac{1}{2}(\hat{B}_{j,k+1} - B_{j,k+1/2}^+ + B_{j,k+1/2}^-) - (\gamma_2)_{j,k+1}
\end{aligned} \tag{26}$$

where $\hat{A} = \hat{A}_1, \hat{B} = \hat{A}_2$ in Eq. (8), and

$$\begin{aligned}
A^\pm &= X_1 \Lambda_1^\pm X_1^{-1} \\
B^\pm &= X_2 \Lambda_2^\pm X_2^{-1}
\end{aligned}$$

Only the orthogonal mesh terms are retained for the implicit viscous terms in order to simplify the left-hand side of the equations. This results in

$$\begin{aligned}
\gamma_1 &= \frac{\nu}{J}(\xi_x^2 + \xi_y^2) I_m \frac{\partial}{\partial \xi} \\
\gamma_2 &= \frac{\nu}{J}(\eta_x^2 + \eta_y^2) I_m \frac{\partial}{\partial \xi}
\end{aligned} \tag{27}$$

The matrix I_m is a modified identity matrix given by

$$I_m = \begin{bmatrix} 0 & 0 & 0 \\ 0 & 1 & 0 \\ 0 & 0 & 1 \end{bmatrix}$$

The numerical system of equations thus formed is solved using a line relaxation method. In this procedure, the entire numerical matrix equation is first formed from values at the previous time level. At this point the numerical equation is stored as a banded matrix of the form

$$\mathcal{B}[V, 0, \dots, 0, X, Y, Z, 0, \dots, 0, W] \Delta D = \hat{R}$$

where $\Delta D = D^{n+1} - D^n$ and $V, W, X, Y,$ and Z are vectors of 3 by 3 blocks which lie on the diagonals of the banded matrix, with the Y vector on the main diagonal. This matrix is

approximately solved using an iterative approach. One family of lines is used as the sweep direction. Using, for example, the ξ family, a tridiagonal matrix is formed by multiplying the elements outside the tridiagonal band by the current ΔD and shifting them over to the right-hand side. This can be represented by the following

$$\mathcal{B}[X, Y, Z](\Delta D)^{l+1} = \hat{R} - \Delta D_{j,k-1}^l V - \Delta D_{j,k+1}^l W$$

where l is an iteration index. This system can be solved most efficiently by first performing and storing the LU decomposition of the tridiagonal matrix before the iteration is begun. Then for each iteration, the right-hand side is formed using the latest known ΔD , and the entire system is backsolved. The LU decomposition can be entirely vectorized, but the backsolution is inherently recursive and cannot be vectorized.

5. Unsteady Formulation

The current scheme can be easily extended to solve unsteady problems with the use of subiterations in pseudo-time at each physical time step. The details of this formulation are given by Rogers and Kwak [3] and by Athavale and Merkle [4], and a short summary of this follows. First, the time derivative in the momentum equations is discretized using a second-order backward Euler formula, resulting in

$$\frac{I_m}{\delta t} \left(1.5\hat{D}^{n+1} - 2\hat{D}^n + 0.5\hat{D}^{n-1} \right) = -R^{n+1}$$

where R is the same residual vector as in Eq. (23). Here physical time is denoted by t and the superscript n denotes the solution at time $t = n\Delta t$. This equation leaves no way to update the pressure to the next time level because of the I_m matrix on the left-hand side. Here the continuity equation is replaced with an artificial compressibility relation and a pseudo-time level is introduced, resulting in

$$I_{t\tau} \left(\hat{D}^{n+1,m+1} - \hat{D}^{n+1,m} \right) = -R^{n+1,m+1} - \frac{I_m}{\Delta t} \left(1.5\hat{D}^{n+1,m} - 2\hat{D}^n + 0.5\hat{D}^{n-1} \right)$$

Here pseudo-time is denoted by τ and the superscript m represents a subiteration index in pseudo-time. The matrix $I_{t\tau}$ is a diagonal matrix given by

$$I_{t\tau} = \text{diag} \left[\frac{1}{\Delta\tau}, \frac{1.5}{\Delta t}, \frac{1.5}{\Delta t} \right]$$

After linearizing the residual about the $n+1, m$ time level, the following equation is obtained

$$\begin{aligned} \left[\frac{I_{t\tau}}{J} + \left(\frac{\partial R}{\partial D} \right)^{n+1,m} \right] \left(\hat{D}^{n+1,m+1} - \hat{D}^{n+1,m} \right) = \\ - R^{n+1,m} - \frac{I_m}{\Delta t} \left(1.5\hat{D}^{n+1,m} - 2\hat{D}^n + 0.5\hat{D}^{n-1} \right) \end{aligned} \quad (28)$$

It can be seen that this equation is very similar to its steady-state counterpart. The additional right-hand side terms and the different diagonal matrix on the left-hand side are the only differences between the two. This makes it quite simple to program a code capable of using this scheme to solve both unsteady and steady-state problems.

6. Boundary Conditions

Implicit boundary conditions are used at all of the boundaries, this helps make possible the use of large time steps. At a no-slip surface, the velocity is specified to be zero, and the pressure at the boundary is obtained by specifying that the pressure gradient normal to the wall be zero. The boundary conditions used for inflow and outflow regions are based on the method of characteristics. The formulation of these boundary conditions is similar to that given by Merkle and Tsai [16], but the implementation is slightly different. The scheme is derived here for a $\xi = \text{constant}$ boundary, with similar results for a $\eta = \text{constant}$ boundary. The finite-speed waves which arise with the use of artificial compressibility are governed by the following

$$\frac{\partial \hat{D}}{\partial \tau} = -\frac{\partial \hat{E}}{\partial \xi} = -\frac{\partial \hat{E}}{\partial D} \frac{\partial D}{\partial \xi} = -\hat{A} \frac{\partial D}{\partial \xi} = -X \Lambda X^{-1} \frac{\partial D}{\partial \xi}$$

then

$$X^{-1} \frac{\partial \hat{D}}{\partial \tau} = -\Lambda X^{-1} \frac{\partial D}{\partial \xi} \quad (29)$$

If one were to move the X^{-1} matrix inside the spatial and time derivative, then it can be seen that this would be a system of scalar equations, each of the form of a wave equation. The sign of the eigenvalues in the Λ matrix determines the direction of travel of the wave. For each positive (negative) eigenvalue, there is a wave propagating information in the positive (negative) ξ direction. The number of positive or negative eigenvalues determines the number of characteristic waves propagating information from the interior of the computational domain to the boundary. Thus these characteristics will be used to bring information from the interior to the boundary. The rest of the information should come from outside the computational domain, and so we are free to specify some boundary conditions.

There will either be one or two characteristics traveling toward the boundary from the interior because there is always at least one positive eigenvalue and one negative eigenvalue. In order to select the proper characteristic waves, Eq. (29) is multiplied by a diagonal selection matrix L which has an entry of one in the position of the eigenvalue we wish to select, and zeros elsewhere. Thus

$$LX^{-1} \frac{\partial \hat{D}}{\partial \tau} = -L\Lambda X^{-1} \frac{\partial D}{\partial \xi} \quad (30)$$

Replacing the time derivative with an implicit Euler time step gives

$$\left(\frac{LX^{-1}}{J\Delta\tau} + L\Lambda X^{-1} \frac{\partial}{\partial \xi} \right) (D^{n+1} - D^n) = -L\Lambda X^{-1} \frac{\partial D^n}{\partial \xi} \quad (31)$$

This gives either one or two relations, depending on the number of non-zero elements in L . To complete the set of equations, some variables must be specified to be constant. Here is defined a vector Ω of the variables to be held constant, such that

$$\frac{\partial \Omega}{\partial \tau} = 0 \longrightarrow \frac{\partial \Omega}{\partial D} \frac{\partial D}{\partial \tau} = 0 \longrightarrow \frac{\partial \Omega}{\partial D} (D^{n+1} - D^n) = 0 \quad (32)$$

Combining Eqs. (31) and (32) gives

$$\left(\frac{LX^{-1}}{J\Delta\tau} + L\Lambda X^{-1} \frac{\partial}{\partial \xi} + \frac{\partial \Omega}{\partial D} \right) (D^{n+1} - D^n) = -L\Lambda X^{-1} \frac{\partial D^n}{\partial \xi} \quad (33)$$

Equation (33) can be used to update the variables implicitly at any of the inflow or outflow boundaries with the proper choice of L and Ω .

6.1 Inflow Boundary

At the inflow, there will be one characteristic wave traveling out of the computational domain since fluid is traveling into the domain. If the incoming fluid is traveling in the positive ξ direction, then

$$\begin{aligned} Q &> 0 \\ Q + c &> 0 \\ Q - c &< 0 \end{aligned}$$

This third eigenvalue will be the one we wish to select, and so L will have a one for the third diagonal entry. If the incoming fluid is traveling in the negative ξ direction, then

$$\begin{aligned} Q &< 0 \\ Q + c &> 0 \\ Q - c &< 0 \end{aligned}$$

and the second eigenvalue is the one corresponding to the wave propagation out of the computational domain, requiring a one in the second diagonal entry of L .

Two different sets of specified variables have been used successfully for inflow boundaries. One set consists of the total pressure and the cross-flow velocity. This set is useful for problems in which the inflow velocity profile is not known. For this set the Ω vector is

$$\Omega = \begin{bmatrix} p + \frac{1}{2}(u^2 + v^2) \\ 0 \\ v \end{bmatrix}; \quad \frac{\partial \Omega}{\partial D} = \begin{bmatrix} 1 & u & v \\ 0 & 0 & 0 \\ 0 & 0 & 1 \end{bmatrix}$$

The second possible set of specified variables consists of the velocity components. This is useful for problems in which a specific velocity profile is desired at the inflow. The Ω vector for this is

$$\Omega = \begin{bmatrix} 0 \\ u \\ v \end{bmatrix}; \quad \frac{\partial \Omega}{\partial D} = \begin{bmatrix} 0 & 0 & 0 \\ 0 & 1 & 0 \\ 0 & 0 & 1 \end{bmatrix}$$

Notice that the row of Ω containing the zero is different in these two cases, the rows have been shifted such that the non-zero rows of the jacobian matrix would have non-zero elements on the diagonal.

6.2 Outflow Boundary

At the outflow boundary there are two characteristic waves traveling out of the computational domain since fluid is also leaving the domain. If the fluid is traveling along the positive ξ direction then

$$\begin{aligned} Q &> 0 \\ Q + c &> 0 \\ Q - c &< 0 \end{aligned}$$

and we require ones in the first two diagonal entries of the L matrix. If the fluid is traveling in the negative ξ direction then

$$\begin{aligned} Q &< 0 \\ Q + c &> 0 \\ Q - c &< 0 \end{aligned}$$

and we require ones in the first and third diagonal entries of the L matrix.

For all of the test problems presented in this paper static pressure was specified at the outflow boundary, resulting in

$$\Omega = \begin{bmatrix} p \\ 0 \\ 0 \end{bmatrix}; \quad \frac{\partial \Omega}{\partial D} = \begin{bmatrix} 1 & 0 & 0 \\ 0 & 0 & 0 \\ 0 & 0 & 0 \end{bmatrix}$$

7. Computed Results

The code was run for three two-dimensional laminar flow test cases. These are first, a driven square cavity flow which has become a standard validation test case due to its simple boundary conditions; second, the flow over a backward facing step which has also become a popular validation case as it is an example of an internal flow with a recirculating region; and third, the flow over a circular cylinder which has become an extensively validated external flow problem. The computing times reported for all cases are the CPU seconds used on a Cray 2 running on one processor. For comparison, these times are nearly the same as obtained running on one processor of a Cray XMP-48. The computations are run until the maximum residual has converged over 6 orders of magnitudes, the maximum divergence of velocity over all the points is less than 10^{-4} , and the flow quantities being measured have approached a steady-state value in at least 4 significant digits. For all cases presented here, the fifth-order upwind flux given in Eq. (20) was used.

For each of the test cases presented, the larger the time step $\Delta\tau$, the better the convergence was. For all cases run with this algorithm, the solutions have always remained

stable independent of the magnitude of $\Delta\tau$. The time step for the present results was set to 10^{12} which effectively reduced the $1/\Delta\tau$ term to zero. The choice of β for each case was arrived at through numerical convergence tests. It was found that the convergence was sensitive to the value of β , and in some cases, extreme values of β could cause the scheme to become unstable. For all cases, however, it was easy to find a range of β for which the code would converge very quickly. This is demonstrated for the case of the flow over a backward facing step. The current scheme was found to be much less sensitive to the value of β than the previous central difference, approximate factorization approach [13], in part because the stability of the previous approach was limited by an approximate factorization error which was a function of β . The convergence of the current formulation is degraded by the errors introduced by the approximate Jacobians on the left hand side of the equations and by the fact that the whole system of equations are not exactly solved by the line-relaxation process. If it were possible to use the exact Jacobians and solve the system exactly then this would be a Newton iteration, in which case one would expect to have quadratic convergence when using a very large time step for any value of β . Analysis of these errors and their relationship to β is underway, and it is hoped that a guideline for choosing β and for minimizing the eigenvalues of the amplification matrix can be obtained. Until such a guideline is found, the numerical tests will have to suffice.

7.1 Driven Cavity Flow

The two-dimensional flow in a driven square cavity whose top wall moves with a uniform velocity has been used rather extensively as a validation test case by many authors in the recent past. It provides a good test case in that there is no primary flow direction and the boundary conditions are very simple to employ. Ghia *et al.* [17] presented extensive numerical data obtained from their multigrid vorticity-stream function formulation using very fine grids. They reported results which agreed quite well with other computational efforts. Other recent computational work involving this particular geometry include Schreiber and Keller [18] who use a vorticity-stream function formulation; Kim and Moin [19] who use a fractional-step method in primitive variables in conjunction with approximate factorization; Vanka [20] who uses a multigrid technique in primitive variables; and Benjamin and Denny [21] who use a centrally-differenced vorticity-stream function formulation in conjunction with an ADI scheme.

The current calculations attempt to maintain the accuracy of these authors while using fewer grid points. The flow is calculated for Reynolds numbers of 100, 400, 1000, 3200, 5000, 7500, and 10,000 using a grid of 81 by 81 points where the points are clustered toward the walls. This grid is shown in Fig. 1. The value of the artificial compressibility β was set to 20 for the Reynolds number of 100, to 10 for the 400 Reynolds number case, to 2 for a Reynolds number of 1000, and was set to 1 for the higher Reynolds numbers. The implicit line relaxation used 11 sweeps in the ξ -direction for each iteration.

The velocity components on the lines passing through the geometric center of the cavity are compared to the results of Ghia *et al.* [17] in Fig. 2. The u-velocity component is plotted along the y-axis for the different Reynolds numbers in Fig. 2a. The origins of the plots has been shifted to the left for each successive Reynolds number case. The data

of Ghia was obtained from a uniform grid of 129 by 129 points for Reynolds numbers up to 3200, and a uniform grid of 257 by 257 points for Reynolds numbers 5000 and greater. It is seen that these two computed results agree very well with each other. In Fig. 2b, the v-velocity component is plotted along the x-axis passing through the geometric center for the different Reynolds numbers. The origins of these plots are shifted up for each successive Reynolds number case. Again, good agreement is seen between the two computed results.

In Table 1, the stream function and vorticity quantities are given for the core of the primary vortex for all the Reynolds numbers. Included with the present results are the results of Ghia *et al.* [17], Schreiber and Keller [18], and Kim and Moin [19]. Listed below the flow quantities is the grid size used for the calculation. Good agreement among all calculations is seen in the lower Reynolds number cases. The discrepancies between different solutions increase at the higher Reynolds numbers, although the same general trend of a leveling off and then a slight decrease in the value of the stream-function is seen.

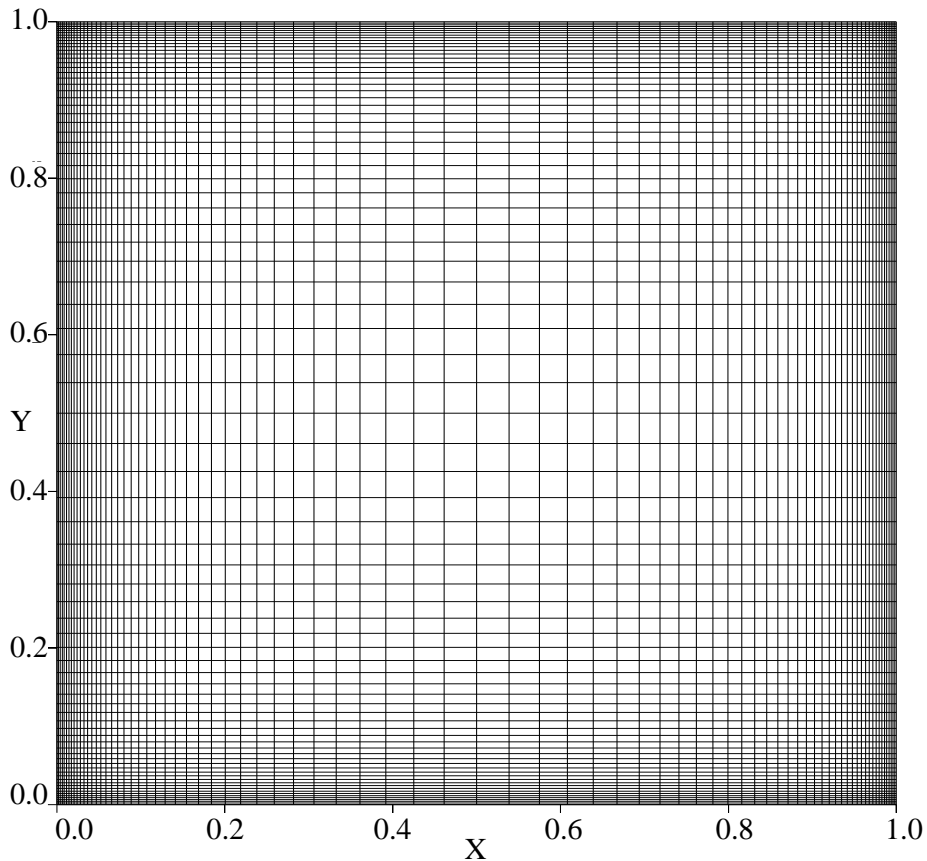


Fig. 1 Grid with 81x81 points used for computing the driven cavity flow.

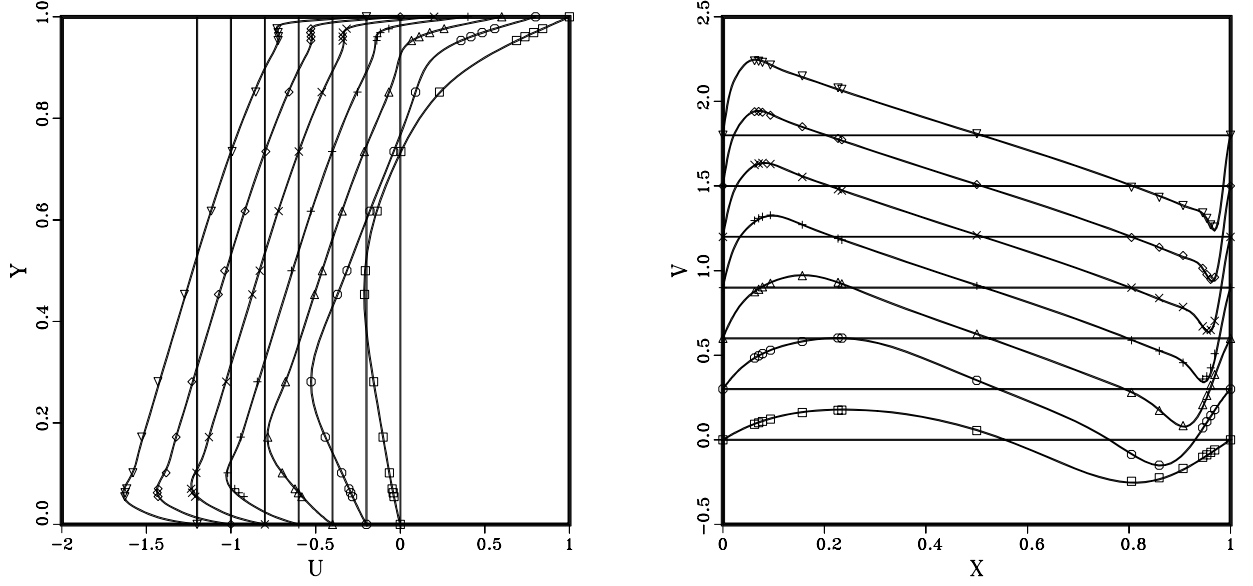


Fig. 2 Comparison between present results (solid line) and computations of Ghia *et al.* [17] (symbols). \square : $Re=100$, \circ : $Re=400$, \triangle : $Re=1000$, $+$: $Re=3200$, \times : $Re=5000$, \diamond : $Re=7500$, and ∇ : $Re=10,000$.

Table 1
Stream-Function and Vorticity at the Center of the
Primary Vortex for Different Reynolds Numbers

Re	Present $\psi_{min} (\omega_{v.c.})$	Ghia <i>et al.</i> [24] $\psi_{min} (\omega_{v.c.})$	Schreiber <i>et al.</i> [25] $\psi_{min} (\omega_{v.c.})$	Kim <i>et al.</i> [6] $\psi_{min} (\omega_{v.c.})$
100	-0.1030(-3.104) 81x81	-0.1034(-3.166) 129x129	-0.1033(-3.182) 121x121	-0.1030(-3.177) 65x65
400	-0.1131(-2.296) 81x81	-0.1139(-2.294) 129x129	-0.1130(-2.281) 141x141	-0.1120(-2.260) 65x65
1000	-0.1171(-2.044) 81x81	-0.1179(-2.050) 129x129	-0.1160(-2.026) 141x141	-0.1160(-2.026) 97x97
3200	-0.1195(-1.904) 81x81	-0.1204(-1.989) 129x129	—	-0.1150(-1.901) 97x97
5000	-0.1192(-1.846) 81x81	-0.1190(-1.860) 257x257	—	-0.1120(-1.812) 97x97
7500	-0.1186(-1.846) 81x81	-0.1200(-1.880) 257x257	—	—
10000	-0.1177(-1.826) 81x81	-0.1197(-1.881) 257x257	-0.1028(-1.622) 180x180	—

To study in more detail the 10,000 Reynolds number case, the streamlines are plotted in Fig. 3. The values of the stream-function contours for this plot are given in Table 2. The contour levels plotted correspond with the values plotted by Ghia *et al.* [17] for this case. Qualitatively, the plots appear to be identical. They each show secondary vortices of the same size and shape in the lower corners and the upper left corner. In Table 3, the stream-function, vorticity, and location of the vortex core for all the secondary vortices for this 10,000 Reynolds number case are given for both the present results and the results of Ghia *et al.* [17]. In this table, the initial T stands for top, B stands for bottom, R stands for right, L stands for left, and the superscript number corresponds to the level of the secondary vortex. Thus BR³ refers to the third and smallest secondary vortex found in the bottom right corner of the cavity. Quite good agreement between the two computations is seen for this case, especially considering that the results of Ghia *et al.* [17] uses over 10 times as many grid points (66,049 versus 6561).

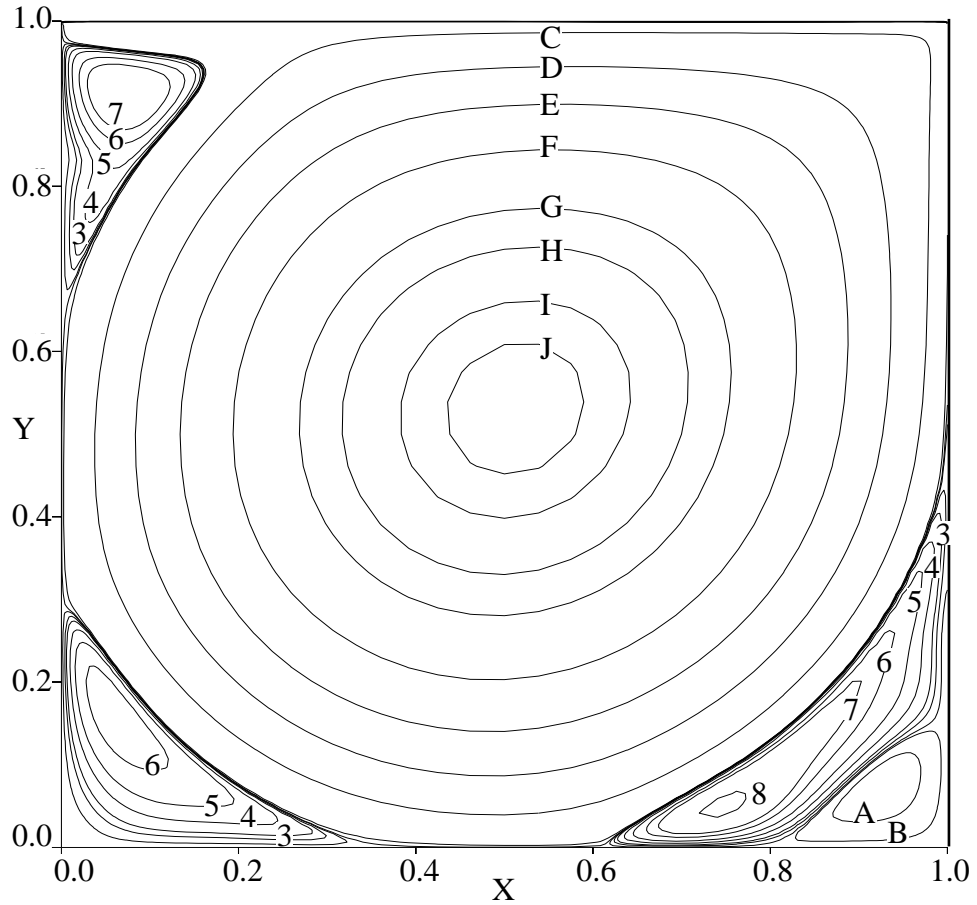


Fig. 3. Streamlines showing the driven cavity flow at $Re = 10,000$.

Table 2
Values for Streamline Contours in Fig. 3

Contour number	Value of ψ	Contour letter	Value of ψ
1	1.0×10^{-5}	A	-1.0×10^{-5}
2	5.0×10^{-5}	B	-1.0×10^{-4}
3	1.0×10^{-4}	C	-0.01
4	2.5×10^{-4}	D	-0.03
5	5.0×10^{-4}	E	-0.05
6	1.0×10^{-3}	F	-0.07
7	1.5×10^{-3}	G	-0.09
8	3.0×10^{-3}	H	-0.1
		I	-0.11
		J	-0.115

Table 3
Properties of the Secondary Vortices for the Driven Cavity at $Re = 10,000$

Vortex	Results	$\psi_{v.c.}$	$\omega_{v.c.}$	$x_{v.c.}$	$y_{v.c.}$
TL	Present	2.418×10^{-3}	2.191	0.0723	0.9117
	Ghia <i>et al.</i> [24]	2.420×10^{-3}	2.183	0.0703	0.9141
BL		1.434×10^{-3}	2.097	0.0585	0.1686
		1.518×10^{-3}	2.086	0.0586	0.1641
BR		3.227×10^{-3}	4.163	0.7619	0.0585
		3.418×10^{-3}	4.053	0.7656	0.0586
BL ²		-5.120×10^{-7}	-0.02207	0.1416	0.01722
		-7.757×10^{-7}	-0.02754	0.1560	0.01950
BR ²		-2.103×10^{-4}	0.3726	0.9277	0.07288
		-1.313×10^{-4}	0.3126	0.9336	0.06250
BR ³		-4.267×10^{-7}	-2.956×10^{-3}	0.9981	0.008697
		-5.668×10^{-9}	–	0.9961	0.003900

The convergence toward a steady-state for this problem was very good for the 3 lowest Reynolds number cases, which required less than 100 iterations and only 35 seconds of computing time. The higher Reynolds number cases were slower to converge, the 10,000 case took 550 iterations and 215 seconds of computing time. The average of the computing requirements for all seven cases came out to 250 iterations and 100 seconds of computing time.

7.2 Flow Over a Backward Facing Step

A second two-dimensional problem which has been used as a validation case is the flow over a backward-facing step. The challenge in modeling this problem comes from the fact that the size of the separation bubbles downstream of the step are very sensitive to the pressure gradient in the flow. The geometry used in the calculations is shown in Fig. 4. At the inflow boundary, a parabolic profile is prescribed throughout the calculation, and the static pressure is allowed to change. Two step-heights downstream from the inflow a two to one expansion is encountered. The outflow boundary extends to 30 step heights downstream of the step. The ability of the flow code to predict the reattachment length, x_1 , of the primary separation bubble behind the step as well as the separation and reattachment locations, x_2 and x_3 , of the secondary separation bubble on the opposite wall was tested by comparing the computed results to experimental values given by Armaly *et al.* [22]. These quantities were measured for the laminar range of Reynolds numbers, which are based on the average inflow velocity and twice the step height. The flow was calculated using a grid of 100 points in the streamwise direction and 53 points in the cross-flow direction. The initial conditions were specified to be freestream velocity at the interior points with uniform pressure everywhere. For the Reynolds numbers of 100 and 200, β was set to 1, for the Reynolds number of 300 case, 0.5 was used, and for the Reynolds numbers of 400 through 800, β was set to 0.1. The implicit line-relaxation process used sweeps along the primary flow direction.

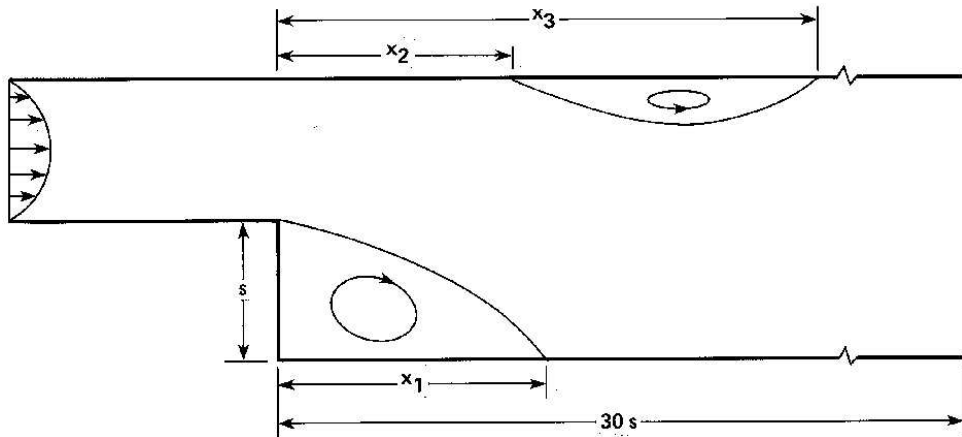


Fig. 4 Geometry of backward-facing step flow problem.

In Fig. 5, the quantities x_1 , x_2 , and x_3 are plotted versus Reynolds number for both the present computed results and the experimental results of Armaly *et al.* [22]. Good agreement is seen between the two for the value of x_1 at the lower Reynolds numbers before the secondary separation appears. At a Reynolds number of 400, the secondary separation bubble is present, and the computed primary reattachment length begins to fall off of the experimental curve. Similarly, the computed secondary separation points are shorter than the experimental values, although the same behavior is seen, that is that the secondary separation point is upstream of the primary reattachment point. The computed secondary reattachment point is seen to be close the experimental values. In their experiment, Armaly *et al.* reported that the flow was found to be three-dimensional

near the step for Reynolds numbers greater than 400, and that the three-dimensional effects were negligible for lower Reynolds numbers. These three-dimensional effects could explain the discrepancies between the calculations and experiment.

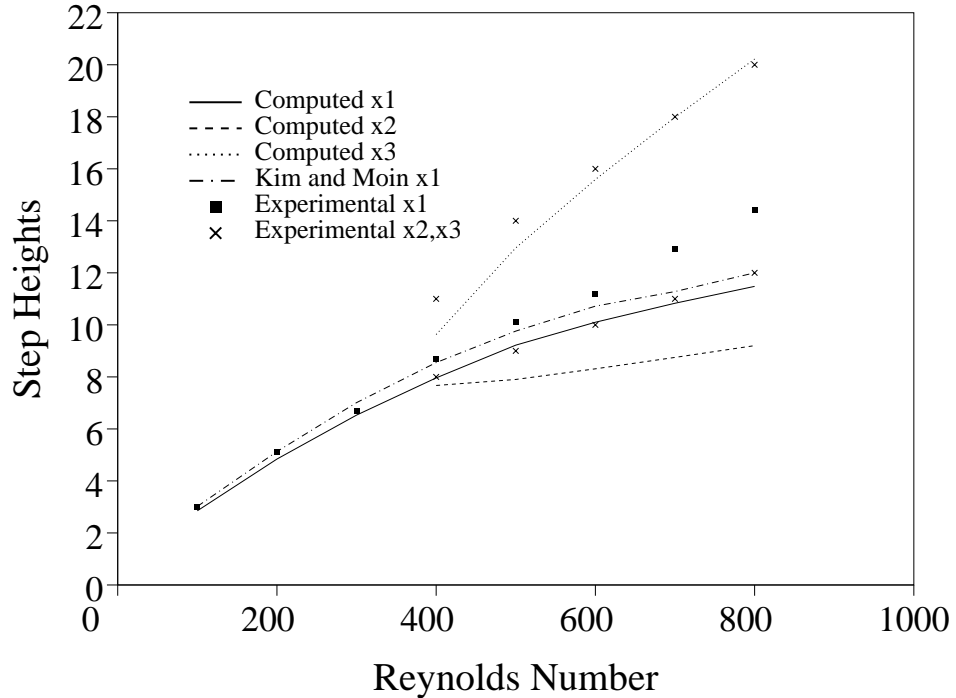


Fig. 5 Separation length versus Reynolds number for the flow over a backward facing step. Solid line: computed x1, dashed line: computed x2, dotted line: computed x3, Δ : experimental x1, $+$: experimental x2, and \times : experimental x3.

Results similar to the present results were reported by Kim and Moin [19]. They reported a primary reattachment length of just under 12 step-heights for a Reynolds number of 800, and the present result for this Reynolds number is 11.48. They reported a secondary separation bubble size of 7.8 and 11.5 step-heights for Reynolds numbers of 600 and 800, respectively. The present results show secondary separation bubble sizes of 7.34 and 11.07 step-heights for these two Reynolds numbers. The similarities between these computational results give credence to the idea that the three-dimensionality of the flow affects the separation bubble size.

The convergence characteristics of the code for this problem are very good. In Fig. 6a the convergence histories for the $Re = 800$ case is plotted for various values of the parameter β . This shows that the convergence is sensitive to the value of β , but that it will produce a solution for a wide range of β . Fig. 6b plots the primary reattachment length $x1$ versus iteration number for the $Re = 100$ and 800 cases. The $Re = 100$ case converges within 55 iterations and the $Re = 800$ case converges within 165 iterations. The average number of iterations required for the 8 different Reynolds number cases is 104 and the average required computing time is just under 11.5 seconds. Comparing this with some of the authors' previous results for a pseudocompressibility approach using central differencing and approximate factorization in a diagonal scheme [13], the present method

produces solutions to the backward-facing step problem much more efficiently. Over the present range of Reynolds numbers, the previous method required on the average of 1500 iterations to converge, and several hundred seconds of computing time. The previous results also reported a larger primary separation region at the higher Reynolds numbers than the current results. The differences are attributed to the fact that the previous results used a coarser grid whose inflow boundary was placed in the plane of the step instead of two step heights upstream as in the current calculations.

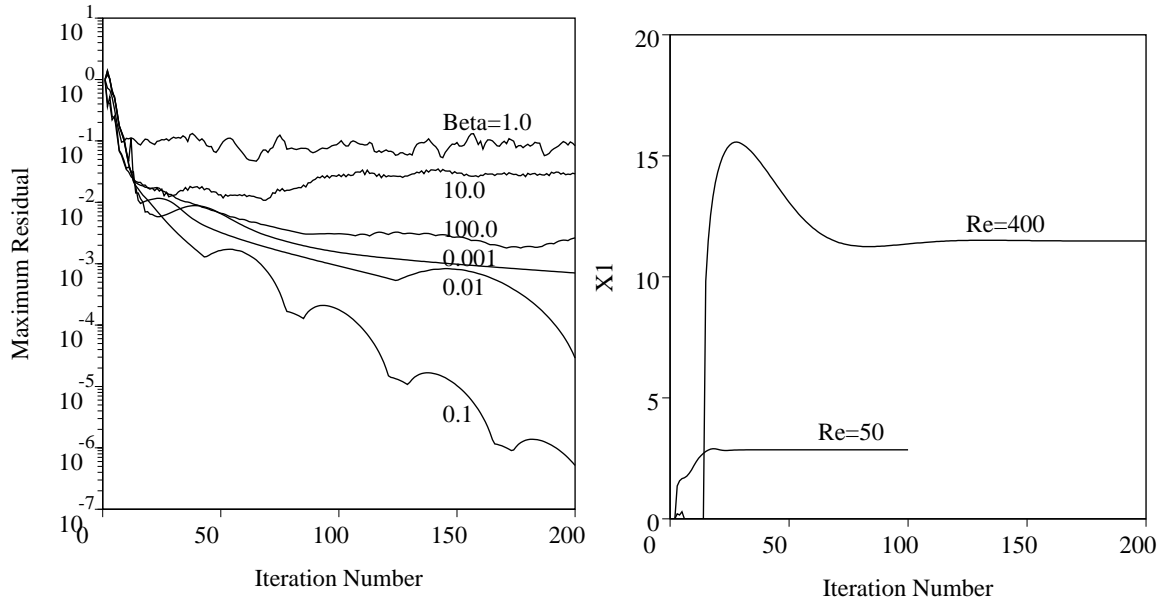


Fig. 6 Convergence history for the flow over a backward facing-step. \triangle : $Re = 100$, \times : $Re = 800$.

7.3 Flow Over a Circular Cylinder

As an example of an external flow problem, the flow over a two-dimensional circular cylinder was calculated. The grid was an algebraically generated o-grid with 100 points in the circumferential direction and 60 points radially. The grid points were clustered radially toward the body and the outer boundary was placed 10 diameters from the cylinder. The code was run and steady-state solutions were obtained for the Reynolds numbers of 5, 10, 20, and 40, based on the freestream velocity and the cylinder diameter. The value of the artificial compressibility constant β was set to 50 for all the cases. At the outer boundary, where fluid was entering the domain, the velocity was held constant, and where fluid was leaving the domain, the static pressure was held constant. The line relaxation scheme used 4 sweeps in both the coordinate directions, which seemed to be the best trade-off of convergence versus computing time in numerical tests.

Table 4
Flow Quantities for a Circular Cylinder

Source	Reynolds Number			
	5	10	20	40
			L_{sep}	
Present	0	0.254	0.932	2.29
[29]	0	0.249	0.935	2.32
[30]	0	0.252	0.94	2.35
[31]	0	0.25	0.9	2.1
[33] (exp)	–	0.34	0.93	2.13
			θ_{sep} (degrees)	
Present	0	28.8	43.1	53.0
[29]	–	29.3	43.7	53.6
[30]	0	29.6	43.7	53.8
[31]	> 6	29.7	44.1	54.8
[32]	–	–	43.6	54.5
[33] (exp)	–	32.5	44.8	53.5
			C_D (C_{Dp})	
Present	4.18 (2.19)	2.89 (1.602)	2.08 (1.242)	1.549 (1.011)
[29]	–	2.80	2.01	1.536
[30]	4.12 (2.20)	2.85 (1.600)	2.05 (1.233)	1.522 (0.998)
[31]	4.66 (2.48)	3.18 (1.775)	2.25 (1.35)	1.675 (1.095)
[32]	–	–	2.18	1.60
[34] (exp)	4.16	3.06	2.02	1.65
			C_{pf} ($-C_{pr}$)	
Present	1.847 (1.067)	1.476 (0.755)	1.265 (0.615)	1.147 (0.536)
[29]	–	1.474 (0.670)	1.261 (0.537)	1.141 (0.512)
[30]	1.872 (1.044)	1.489 (0.742)	1.269 (0.589)	1.144 (0.509)
[31]	2.23 (1.081)	1.744 (0.773)	1.457 (0.614)	1.312 (0.543)

For each case, several flow quantities of the flow were computed. Fig. 7 shows a schematic diagram of the geometry for this flow problem along with several of these flow quantities. These quantities are the flow separation length measured from the rear of the cylinder in cylinder diameters (L_{sep}), the angle which defines the point of separation from the body (θ_{sep}), the coefficient of drag (C_D), the coefficient of pressure drag (C_{Dp}), the coefficient of pressure at the front (C_{pf}) and rear (C_{pr}) stagnation points. In Table 4, these quantities are presented for the present calculations as well as the numerical results

of Takami and Keller [23], Dennis and Chang [24], Tuann and Olson [25], Braza *et al* [26], and the experimental results of Coutanceau and Bouard [27] and of Tritton [28]. The comparisons show that there is very good agreement among nearly all of the results.

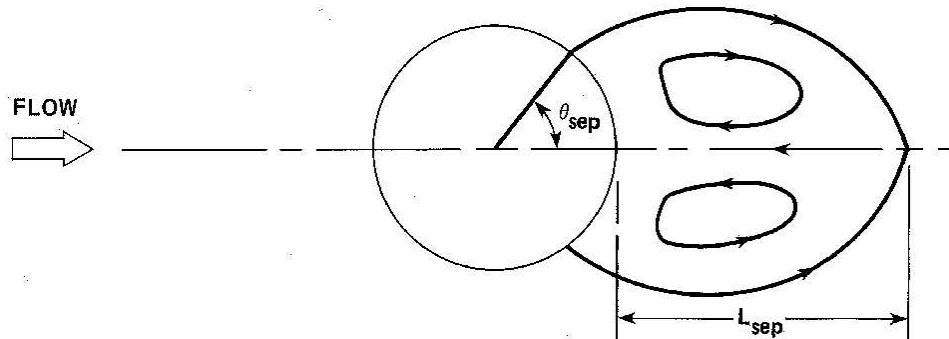


Fig. 7 Schematic diagram showing flow quantities for the circular cylinder flow computations.

The convergence of the code toward a steady-state solution for the problem of a circular cylinder was found to be quite good. All four Reynolds number cases converged in less than 70 iterations, requiring an average of 21 seconds of computing time.

8. Summary

The use of a flux-difference split upwind differencing scheme has been applied to the artificial compressibility equations to solve the steady-state Navier-Stokes equations. This eliminates the need for any explicitly added artificial dissipation terms and any artificial dissipation coefficients. This code has been found to be much more robust and easier to run than previous applications by the authors of the artificial compressibility method which used central differencing plus artificial dissipation. The natural addition of dissipation through the use of upwind-biased stencils requires no trial-and-error adjusting of smoothing parameters as does the artificial dissipation. As well, it is thought that the terms on the main diagonal of the implicit side matrix which are not present in the central difference scheme make the scheme much more robust. Implicit boundary conditions based on the method of characteristics were presented. The accuracy of the upwind scheme has been established using three two-dimensional test cases. Good comparison was found between the current method and other methods which used many more grid points in calculating the flow inside a driven cavity. Results which compared well with experimental values were obtained in calculating the flow over a backward facing step. The discrepancy at higher Reynolds numbers could be explained by the three-dimensionality of the experiment, and this was supported by other computational results. Finally, good comparison was found in measuring the flow around a circular cylinder. Perhaps the most striking feature of the current code is it's ability to obtain steady-state solutions in a small number of iterations for most problems. Very good convergence rates were observed when the proper choice of the artificial compressibility constant β was made. No analytical guidelines for the choice of this parameter have been derived as yet, and this is a subject of on going work. The

extension of the current code to three-dimensions is currently being validated and has been found to be straight forward.

Acknowledgements

This work was partially sponsored by NASA Marshall Space Flight Center.

References

1. A. J. Chorin, "A Numerical Method for Solving Incompressible Viscous Flow Problems," *J. Comput. Phys.* **2** (1967), 12.
2. D. Kwak, J. L. C. Chang, S. P. Shanks, and S. R. Chakravarthy, "A Three-Dimensional Incompressible Navier-Stokes Flow Solver Using Primitive Variables," *AIAA J.*, **24**(3) (1986), 390.
3. S. E. Rogers and D. Kwak, "An Upwind Differencing Scheme For The Time-Accurate Incompressible Navier-Stokes Equations," *AIAA J.*, **28**(2) (1990), 253.
4. M. M. Athavale and C. L. Merkle, "An Upwind Differencing Scheme For Time-Accurate Solutions of Unsteady Incompressible Flow," AIAA Paper 88-3650, 1988.
5. S. E. Rogers, D. Kwak, and U. K. Kaul, "A Numerical Study of Three-Dimensional Incompressible Flow Around Multiple Posts," *Appl. Math. Modelling*, **11** (1987), 35.
6. S. R. Chakravarthy, and S. Osher, "A New Class of High Accuracy TVD Schemes For Hyperbolic Conservation Laws," AIAA Paper 85-0363, 1985.
7. P. L. Roe, "Approximate Riemann Solvers, Parameter Vectors, and Difference Schemes," *J. Comput. Phys.*, **43** (1981), 357.
8. J. L. Steger, and R. F. Warming, "Flux Vector Splitting of the Inviscid Gasdynamic Equations With Application to Finite Difference Methods," NASA TM 78605.
9. A. Harten, P. D. Lax, and B. Van Leer, "On Upstream Differencing and Godunov-Type Schemes for Hyperbolic Conservation Laws," *Siam Review*, **25**(1) (1983), 35.
10. P. M. Hartwich, and C. H. Hsu, "High Resolution Upwind Schemes For The Three-Dimensional Incompressible Navier-Stokes Equations," AIAA Paper 87-0547, 1987.
11. C. H. Hsu, and P. M. Hartwich, "Incompressible Navier-Stokes Solutions For a Sharp-Edged Double-Delta Wing," AIAA Paper 87-0206, 1987.

12. J. J. Gorski, "TVD Solution of the Incompressible Navier-Stokes Equations With An Implicit Multigrid Scheme," AIAA Paper 88-3699, 1988.
13. S. E. Rogers, J. L. C. Chang, and D. Kwak, "A Diagonal Algorithm For The Method of Pseudocompressibility," *J. Comput. Phys.* **73**(2) (1987), 364.
14. M. M. Rai, "Navier-Stokes Simulations of Blade-Vortex Interaction Using High-Order Accurate Upwind Schemes," AIAA Paper 87-0543, 1987.
15. T. J. Barth, "Analysis of Implicit Local Linearization Techniques For Upwind And TVD Algorithms," AIAA Paper 87-0595, 1987.
16. C. L. Merkle and P. Y. L. Tsai, "Application Of Runge-Kutta Schemes to Incompressible Flows," AIAA Paper 86-0553, 1986.
17. U. Ghia, K. N. Ghia, and C. T. Shin, "High-Re Solutions for Incompressible Flow Using the Navier-Stokes Equations and a Multigrid Method," *J. Comput. Phys.* **48** (1982), 387.
18. R. Schreiber and H. B. Keller, "Driven Cavity Flows by Efficient Numerical Techniques," *J. Comput. Phys.* **49** (1983), 310.
19. J. Kim and P. Moin, "Application of a Fractional-Step Method to Incompressible Navier-Stokes Equations," *J. Comput. Phys.* **59** (1985), 308.
20. S. P. Vanka, "Block-Implicit Multigrid Solution of Navier-Stokes Equations in Primitive Variables," *J. Comput. Phys.* **65** (1986), 138.
21. A. S. Benjamin and V. E. Denny, "On the Convergence of Numerical Solutions for 2-D Flows in a Cavity at Large Re," *J. Comput. Phys.* **33**, (1979), 340.
22. B. F. Armaly, F. Durst, J. C. F. Periera, and B. Schönung, "Experimental and Theoretical Investigation of Backward-Facing Step Flow," *J. Fluid Mech.* **127** (1983), 473.
23. H. Takami and H. B. Keller, "Steady Two-Dimensional Viscous Flow of an Incompressible Fluid Past a Circular Cylinder, *Phys. Fluids Suppl. II* **12** (1969), II-51.
24. S. C. R. Dennis and G. Z. Chang, "Numerical Solutions for Steady Flow Past a Circular Cylinder at Reynolds Numbers up to 100," *J. Fluid Mech.* **42** (1970), 471.
25. S. Y. Tuann and M. D. Olson, "Numerical Studies of the Flow Around a Circular Cylinder by a Finite Element Method," *Comp. and Fluids*, **6** (1978), 219.
26. M. Braza , P. Chassaing, and H. Ha Minh, "Numerical Study and Physical Analysis of the Pressure and Velocity Fields in the Near Wake of a Circular Cylinder," *J. Fluid*

Mech. **165** (1986), 79.

27. M. Coutanceau and R. Bouard, "Experimental Determination of the Main Features of the Viscous Flow in the Wake of a Circular Cylinder in Uniform Translation. Part 1. Steady Flow," *J. Fluid Mech.* **79(2)** (1977), 231.
28. D. J. Tritton, "Experiments on the Flow Past a Circular Cylinder at Low Reynolds Numbers," *J. Fluid Mech.* **6** (1959), 547.